



HAL
open science

Simple synthesis and characterization of vertically aligned Ba_{0.7}Sr_{0.3}TiO₃ –CoFe₂O₄ multiferroic nanocomposites from CoFe₂ nanopillar arrays

Sergey Basov, Catherine Elissalde, Quentin Simon, Mario Maglione, Christopher Castro-Chavarria, Thomas Herrison de Beauvoir, Sandrine Payan, Kristiaan Temst, Vera Lazenka, Vlad Andrei Antohe, et al.

► To cite this version:

Sergey Basov, Catherine Elissalde, Quentin Simon, Mario Maglione, Christopher Castro-Chavarria, et al.. Simple synthesis and characterization of vertically aligned Ba_{0.7}Sr_{0.3}TiO₃ –CoFe₂O₄ multiferroic nanocomposites from CoFe₂ nanopillar arrays. *Nanotechnology*, 2017, 28 (47), pp.475707. 10.1088/1361-6528/aa9016 . hal-01734809

HAL Id: hal-01734809

<https://hal.science/hal-01734809>

Submitted on 19 Feb 2021

HAL is a multi-disciplinary open access archive for the deposit and dissemination of scientific research documents, whether they are published or not. The documents may come from teaching and research institutions in France or abroad, or from public or private research centers.

L'archive ouverte pluridisciplinaire **HAL**, est destinée au dépôt et à la diffusion de documents scientifiques de niveau recherche, publiés ou non, émanant des établissements d'enseignement et de recherche français ou étrangers, des laboratoires publics ou privés.

Simple synthesis and characterization of vertically aligned $\text{Ba}_{0.7}\text{Sr}_{0.3}\text{TiO}_3\text{-CoFe}_2\text{O}_4$ multiferroic nanocomposites from CoFe_2 nanopillar arrays

Sergey Basov,^{1,3} Catherine Elissalde,¹ Quentin Simon,¹ Mario Maglione,¹ Christopher Castro-Chavarria,¹ Thomas Herrison de Beauvoir,¹ Sandrine Payan,¹ Kristiaan Temst,² Vera Lazenka,² Vlad Andrei Antohe,³ Pedro Miguel Pereira de Sá,³ David Sallagoity^{1,3} and Luc Piraux³

¹Institut de Chimie de la Matière Condensée de Bordeaux, Université de Bordeaux, UPR-CNRS 9048, Avenue du Docteur Schweitzer 87, F-33600 Pessac, France

²Instituut voor Kern- en Stralingsfysica, KU Leuven, Celestijnenlaan 200D, B-3001 Leuven, Belgium

³Institute of Condensed Matter and Nanosciences, Université catholique de Louvain, Place Croix du Sud 1, B-1348 Louvain-la-Neuve, Belgium

E-mail : luc.piraux@uclouvain.be

Abstract.

A new strategy to elaborate (1-3) type multiferroic nanocomposites with controlled dimensions and vertical alignment is presented. The process involves a supported nanoporous alumina layer as a template for growth of free-standing and vertically aligned CoFe_2 nanopillars using a room temperature pulsed electrodeposition process. $\text{Ba}_{0.70}\text{Sr}_{0.30}\text{TiO}_3\text{-CoFe}_2\text{O}_4$ multiferroic nanocomposites were grown through direct deposition of $\text{Ba}_{0.7}\text{Sr}_{0.3}\text{TiO}_3$ films by radio-frequency sputtering on the top surface of the pillar structure, with in-situ simultaneous oxidation of CoFe_2 nanopillars. The vertically aligned multiferroic nanocomposites were characterized using various techniques for their structural and physical properties. The large interfacial area between the ferrimagnetic and ferroelectric phases leads to a magnetoelectric voltage coefficient as large as $\sim 320 \text{ mV cm}^{-1} \text{ Oe}^{-1}$ at room temperature. This simple method has great potential for large-scale synthesis of many other hybrid vertically aligned multiferroic heterostructures.

1. Introduction

Multiferroic nanostructured composites have attracted a lot of attention due to the control of the extrinsic coupling between polarization and magnetization via strain [1-4] and their potential application in memory, actuators, sensors, and microwave devices [2, 5]. Intensive research in the field of multiferroic nanocomposites has opened new routes such as the fabrication of vertically aligned nanostructures, i.e. nanopillars embedded in a matrix, the so called (1-3) connectivity nanocomposite. These types of nanostructures offer the advantage to reduce the

substrate imposed clamping effect, as compared to multilayered (2-2) types of multiferroic nanocomposites, and to enhance the interfacial area between the two phases, so that large magnetoelectric (ME) coupling can be expected [2, 6]. Up to now, vertically aligned multiferroic nanostructures from spinel and perovskite systems, including $\text{CoFe}_2\text{O}_4\text{-BaTiO}_3$ (CFO-BTO) and $\text{CoFe}_2\text{O}_4\text{-BiFeO}_3$ (CFO-BFO) were fabricated using pulsed laser deposition (PLD) techniques [7, 8]. In order to control the long-range ordered vertical interface, anodic aluminium oxide (AAO) membranes were used as a hard mask to grow columnar multiferroic nanocomposites [9]. Thick

AAO membranes were also used as templates to fabricate multiferroic core-shell nanowire arrays using a combination of different synthesis processes, such as sol-gel processing, electrodeposition, and thermal annealing [10, 11]. However, to our best knowledge, there is no report on the fabrication of vertically aligned multiferroic nanocomposites based on a direct sputtering deposition of the ferroelectric film onto the top surface of the vertically aligned free-standing metallic nanopillar array structure grown by electrodeposition into AAO masks supported on silicon (Si) substrates.

In this work, we demonstrate a simple approach to synthesize vertically aligned $\text{Ba}_{0.7}\text{Sr}_{0.3}\text{TiO}_3\text{-CoFe}_2\text{O}_4$ (BSTO-CFO) nanocomposites with increased interfacial area between the ferroelectric and ferrimagnetic components. The $\text{Ba}_x\text{Sr}_{1-x}\text{TiO}_3$ material is chosen due to the tunable Curie temperature (T_C), accompanied by the large dielectric permittivity through a variation of the $\text{BaTiO}_3/\text{SrTiO}_3$ composition, e.g. for the composition 70 at% Ba ($x \sim 0.7$) T_C is close to room temperature [12]. The fabrication process starts with the growth of free-standing and vertically aligned metallic CoFe_2 nanopillar arrays using pulsed electrochemical deposition inside nanopores of anodized AAO templates on Si substrates followed by a dissolution of the template. Then, BSTO-CFO film nanostructures are formed by direct deposition by radio frequency (rf) magnetron sputtering with Ar/O_2 reactive plasma of the BSTO matrix onto the CoFe_2 nanopillar arrays with in-situ oxidation to form the desired oxidized CFO phase. This original in-situ synthesis of vertically aligned multiferroic nanostructures allows us to improve the ordering of the magnetic nanopillars inside the matrix, and to preserve the nanopillar morphology. Indeed, when the oxidation of the free-standing CoFe_2 nanopillars was conducted by thermal treatment prior to BSTO deposition, a significant change of the surface roughness morphology of the pillars, and an increase of their diameter were found, thus preventing the penetration of BSTO through the ordered pillar arrays. We used different techniques to characterize the electrical and magnetic properties and to quantify the magnetoelectric coefficient of the resulting BSTO-CFO multiferroic nanostructures.

2. Experimental details

High quality analytical grade (99.99%, unless otherwise specified) chemicals were used in this work

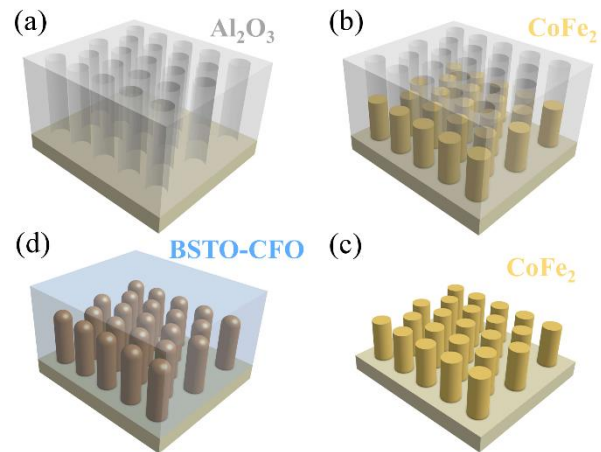


Figure 1. Sketch of the fabrication process of the vertically aligned BSTO-CFO nanostructures: (a) anodized AAO template supported on a Pt/Ti/Si substrate, (b) CoFe_2 nanopillars obtained by electrodeposition into the AAO nanoporous structure, (c) free-standing CoFe_2 nanopillar array obtained after chemical dissolution of the AAO template, (d) vertically aligned multiferroic BSTO-CFO nanostructures made by deposition of the BSTO layer onto the CoFe_2 pillar structure using rf magnetron sputtering with their simultaneous oxidation into a CFO nanopillar array.

as provided, without further purification. The aqueous solutions were prepared with ultra-pure deionized water (DIW) purchased from VWR Chemicals, France. The close-packed array of the vertically aligned CoFe_2 nanopillars was produced by an electrochemical deposition within nanopores of the supported AAO template (figure 1), following a slightly modified protocol as previously reported [13, 14]. In brief, a freshly cleaned Si substrate was first prepared by depositing an ultra-compact Al film ($\sim 1 \mu\text{m}$) over an intermediate Ti/Pt/Ti under-layer ($\sim 5/50/5 \text{ nm}$), by magnetron sputtering (Plassys MP500S). Pt was used for a two-fold purpose: (1) to prevent nanopillar contamination via diffusion during the subsequent thermal treatment and (2) to serve as a bottom electrode for electrodeposition and physical measurements. The as-prepared Al/Ti/Pt/Ti/Si substrate was then exposed to a single step anodization process in 0.3 M oxalic acid ($\text{H}_2\text{C}_2\text{O}_4$) at 2°C , by applying an anodic potential of 60 V from a Keithley 2400 sourcemeter, followed by a chemical widening of the nanopores in a 0.5 M sulphuric acid (H_2SO_4) solution (Merck, Germany) at 40°C for 1 hour. The resulting AAO film had a thickness of $\sim 1.4 \mu\text{m}$ with a nanopore interspacing $\sim 150 \text{ nm}$ (the distance from center to center of nanopores) and an average pore diameter $\sim 90 \text{ nm}$, generating a porosity factor $P \sim 35\%$ [15]. In the second stage, CoFe_2 alloy nanopillars were grown into the nanopores of the supported AAO

template with a pulsed potentiostatic electrodeposition method. The CoFe₂ nanopillars were electrodeposited at ambient temperature from a single water-based electrolyte containing 0.1 M CoSO₄ · 7H₂O (98%, Alfa Aesar, Germany), 0.14 M FeSO₄ · 7H₂O (Merck, Germany), and 0.16 M H₃BO₃ (99.5%, Sigma-Aldrich, MO) in a standard three-electrode potentiostatic configuration using a PAR 263A Potentiostat/Galvanostat and a Pt foil as a counter electrode. The operating potential stepped from -1.5 V (versus Ag/AgCl reference electrode) during 20 milliseconds and -0.5 V during 80 milliseconds. The height of the nanopillars was easily controlled by varying the charge-controlled electrodeposition duration. The AAO template was then dissolved in 2 M of sodium hydroxide NaOH solution (Merck, Germany) during 20 minutes and washed in distilled water, thus leading to a free-standing and vertically aligned CoFe₂ nanopillar arrays on the Pt/Ti/Si substrate (figure 1(c)). Nanopillar arrays having an average height of ~200 nm were considered. The Ba_{0.7}Sr_{0.3}TiO₃ (BSTO) matrix was deposited by rf magnetron sputtering (Plassys MP700) in facing target configuration (90° off-axis geometry) using two home-made BSTO targets (rf power = 75 W) and reactive Ar/O₂ plasma (5 Pa and 1% O₂). Upon deposition, the substrates were kept at 650 °C with a substrate-to-target distance close to 40 mm. The deposition time was adjusted to fill the internal space of the pillar arrays as well as to obtain the desired BSTO layer thickness around 250 nm at the top of the nanopillar structure. Finally, Pt top electrodes having approximate diameters of 300 μm and 600 μm were deposited on the surface of the nanocomposites by rf magnetron sputtering through a shadow mask for the dielectric and magnetoelectric characterizations.

Surface morphology was investigated using a high-resolution scanning electron microscopy JEOL 7600F (SEM) equipped with an energy dispersive X-ray (EDX) analyser. The crystal structure of the nanocomposites was characterized using a Bruker D8 Discover diffractometer in grazing incidence X-Ray diffraction configuration (GIXRD), operating with CuKα radiation (CuKα₁ = 1.5406 Å, CuKα₂ = 1.5443 Å) and with an incident beam angle of 2°. Room temperature magnetic properties of the CoFe₂ and the BSTO-CFO nanostructures were investigated using an alternating gradient magnetometer (PMC MicroMag AGM) with a maximum magnetic field of ±14 kOe. The dielectric properties (capacitance and loss tangent) were measured as a function of temperature (from 80

K to 400 K), frequency (from 100 Hz to 1 MHz), and bias voltage (with a maximum electric field ±5 V) using a HP 4194A impedance analyser. The effective permittivity of the deposits was calculated as

$$\varepsilon = \frac{C \times t}{\varepsilon_0 \times S}$$

using the measured capacitance value C , $\varepsilon_0 \approx 8.854 \times 10^{-12}$ F/m, the top Pt electrode surface area S , and the total thickness of the deposit t , assuming that the nanocomposite can be considered as a continuous material. The ME voltage coefficient was measured using a Quantum Design physical property measurement system (PPMS). The ac voltage induced across the BSTO-CFO capacitor structure (δE) in response to a small ac magnetic field ($\delta H = 10$ Oe), generated in coil at a fixed frequency of 1 kHz, was measured with a lock-in amplifier (Stanford Research Systems, SR 830). Both the ac and dc magnetic fields (up to 4 Tesla) were applied in out-of-plane direction (perpendicular to the nanostructure plane) and in the same direction as the measured ME voltage response. The ME coefficient was calculated using the relation

$$\alpha_E = \frac{\delta E}{\delta H} = \frac{\delta V}{t \times \delta H} = \frac{V_{ac}}{t \times H_{ac}}$$

where V_{ac} is the magnetically induced ac electric voltage across the sample, and t is the sample thickness.

3. Results and discussion

A tilted-view SEM image of the vertically aligned and free-standing CoFe₂ nanopillar arrays on Pt/Ti/Si substrate, obtained after removal of the AAO template, is shown in figure 2(a). The nanopillars height is ~200 nm and diameter ~90 nm, as expected from the morphological features of the porous AAO template. An average chemical analysis was provided by EDX (not shown) confirming a value of the Fe/Co ratio close to 2. Both ordering and uniformity in diameter of the CoFe₂ nanopillars can be seen on the top-view SEM image (figure 2(b)). A tilted-view SEM image (figure 2(c)) of the BSTO-CFO nanostructure shows that the BSTO matrix penetrates the spacing between the pillars to form the two-phase columnar structure made of the CFO pillars coated by the BSTO shells (schematically represented in figure 2(c)). A continuous BSTO layer of thickness ~250 nm is also formed at the top of the CFO nanopillars with a rather high surface roughness (figures 2(c) and

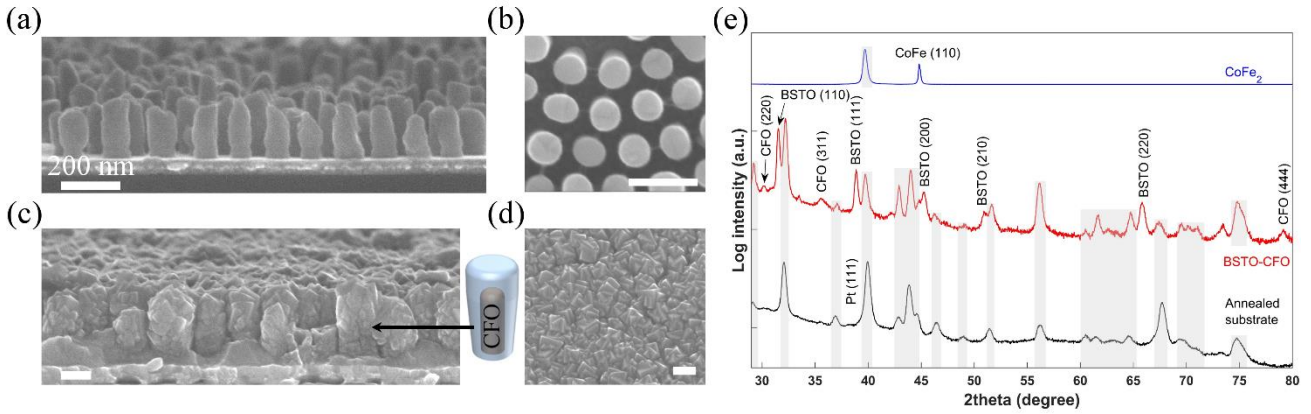


Figure 2. Tilted-view and top-view SEM images of a vertically aligned CoFe_2 nanopillar array (a, b), SEM images of the samples corresponding to a tilted-view and a top-view on the BSTO-CFO nanostructure (c, d). The scale bar corresponds to ~ 200 nm. (e) GIXRD patterns of the vertically aligned CoFe_2 nanopillar arrays (blue), the BSTO-CFO nanostructure (red), and the Pt/Ti/Si substrate annealed at ~ 600 °C (black).

2(d)). The total thickness of the BSTO-CFO nanostructure is about 500 nm, which is larger than the sum of the CoFe_2 nanopillars height and the top BSTO layer thickness indicating the volume expansion of the nanopillars. Similar volume expansion was observed after the thermal treatment of the free-standing CoFe_2 nanopillar arrays.

The critical step to achieve BSTO-CFO nanostructure is clearly the in-situ oxidation of the CoFe_2 metallic pillars during BSTO deposition. Both structural and magnetic characterization have been conducted to probe the oxidation efficiency of the nanopillar arrays. Figure 2(e) shows GIXRD patterns of the BSTO-CFO nanostructure, the CoFe_2 nanopillar arrays (JCPDS # 48-1816), and the Pt/Ti/Si substrate annealed at ~ 600 °C (temperature selected close to the one used for the sputtering process). The oxidation of the CoFe_2 nanopillar array into a polycrystalline CFO nanopillar array during the BSTO matrix deposition was confirmed by XRD through the appearance of the CFO peaks (220), (311), and (444) (JCPD # 22-1086). Note that the (222), (440) and (511) – peaks are not visible because the phases corresponding to CFO and the annealed substrate can hardly be discriminated. The diffraction patterns of the BSTO-CFO nanostructure confirm the crystallization of the BSTO matrix with all peaks corresponding to the perovskite structure. Pt peaks and additional peaks resulting from reactions and associated phase formation during annealing are observed in the XRD pattern of the Pt/Ti/Si substrate.

Figures 3(a) and 3(b) show the normalized magnetic hysteresis loops measured at room temperature with the field applied along the in-plane

(perpendicular to pillar axis) and out-of-plane (parallel to pillar axis) directions. The effective magnetic anisotropy in a nanopillar array in the saturated state is determined by different contributions, namely shape anisotropy, dipolar inter-pillar coupling and magnetocrystalline anisotropy [16]. For the CoFe_2 nanowire array, the magnetocrystalline anisotropy can be neglected and the effective anisotropy is entirely magnetostatic, as pointed out previously [17]. Figure 3(a) reveals the easy axis of magnetization along the in-plane direction, as shape anisotropy, associated with the infinite array of the vertically aligned nanopillars behaving as a whole film, overcomes the uniaxial shape anisotropy along the out-of-plane direction of the individual nanopillars due to the high packing density and relatively small aspect ratio of the individual nanopillars [18]. In addition, this causes the coercivity $H_c \sim 190$ Oe and the remanence-saturation ratio ~ 0.08 to become relatively small, irrespective of the direction of the applied field. Figure 3(b) shows the magnetic hysteresis curve for the embedded CoFe_2O_4 nanowire array in the BSTO matrix. The shapes of the

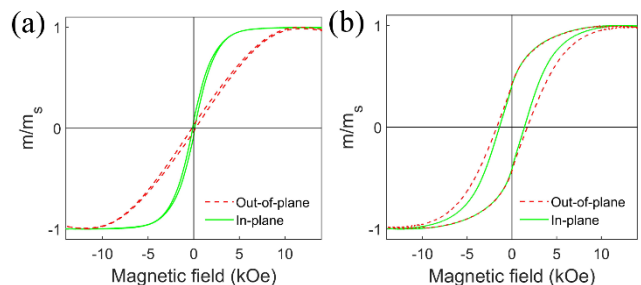


Figure 3. Room temperature hysteresis loops along in-plane (solid line) and out-of-plane (dashed line) directions for a vertically aligned CoFe_2 nanopillar array (a) and the BSTO-CFO multiferroic nanostructure (b). The magnetic moment is normalized to its value in the saturation state.

hysteresis loops are similar in the in-plane and out-of-plane directions, thus indicating the absence of magnetic anisotropy. This can be ascribed to the fact that the magneto-crystalline anisotropy energy dominates in the CFO nanopillar arrays, and there is no preferred crystallite orientation along the wire axes. Besides, large coercive field ($H_c \sim 1.7$ kOe) and remanence ($m/m_s \sim 0.44$) have been achieved in the BSTO-CFO multiferroic nanostructure. Such high coercive field is associated with the large magnetocrystalline anisotropy, and also possibly since the grain size is approaching the single-domain critical value [19]. The coercive fields for CFO nanowires are comparable to the room temperature values reported in the literature, thus confirming the efficacy of the in-situ oxidation of the CoFe_2 nanopillars during the deposition of the BSTO matrix [19]. We also found that the experimentally measured magnetic moment of the metal nanopillar array decreased by a factor of 3.15 after the in-situ oxidation. Taking into account the approximate oxidation-induced volume expansion (~ 1.5) of the nanowires, this reduction of the sample's magnetic moment roughly corresponds to a large reduction in the saturation magnetization by a factor 4.7. This result is in good agreement with the expected ratio between the saturation magnetization for the CoFe_2 (~ 1940 emu/cm³) and CFO (~ 400 emu/cm³) bulk materials at room temperature [20, 21].

A macroscopic evidence of ferroelectricity is a prerequisite to expect magnetoelectric coupling in such BSTO-CFO nanostructured composites. However, this remains challenging considering the complexity of these vertically aligned heterostructures. Dielectric investigations were performed, taking the well-behaved BSTO thin film as a reference for the BSTO-CFO nanostructures. Since the geometry of both sets of samples is quite different, only the capacitance and dielectric losses will be compared in the following.

Figure 4 shows the thermal variations at three frequencies (10 kHz, 100 kHz, and 1 MHz) of capacitance and dielectric losses for both a pure BSTO thin film (figures 4(a) and 4(b)) and the BSTO-CFO nanostructure (figures 4(c) and 4(d)). The pure BSTO thin film exhibits a broad $C(T)$ anomaly in a wide range of temperature, corresponding to a diffuse ferroelectric-to-paraelectric transition (figure 4(a)). This diffuse behaviour is associated with a maximum of the capacitance occurring at lower temperature (250 K) compared to the ceramic counterpart ($T_C \sim 310$ K for the bulk $\text{Ba}_{0.7}\text{Sr}_{0.3}\text{TiO}_3$), as commonly observed for

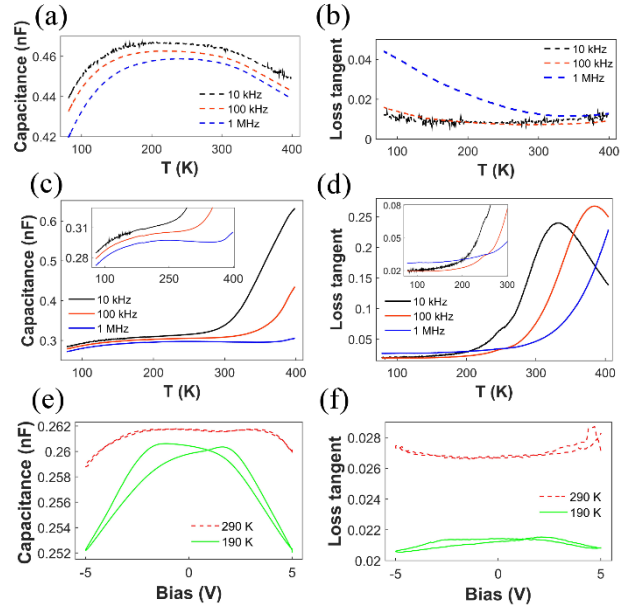


Figure 4. Capacitance and dielectric losses as a function of temperature for the BSTO thin film with thickness ~ 250 nm (a, b) and the BSTO-CFO nanostructure capacitor (c, d), capacitance and dielectric losses (e, f) as a function of bias voltage for the BSTO-CFO nanostructure at two distinct temperatures, $T = 190$ K and $T = 290$ K

thin films [12, 22]. These discrepancies can arise from the microstructure of ferroelectric thin films including small grain size, residual strain and interfacial contributions [22, 23]. Therefore, the ferroelectric properties of the BSTO thin film are still partially present at room temperature. Over the whole temperature range, the dielectric losses of the BSTO thin film remain below ~ 0.05 (figure 4(b)). For the BSTO-CFO nanostructure, the capacitance slightly increases when the temperature is raised from 80 to 200 K, similar to the pure BSTO thin film (see figure 4(c) and inset). However, the maximum in capacitance associated with the ferroelectric-to-paraelectric transition close to 250 K can only be observed at high frequency ~ 1 MHz. At lower frequency this maximum is hindered by a strong increase of the apparent capacitance above 200 K. Accordingly, the dielectric losses showed pronounced peaks (figure 4(d)), whose maximum is shifted to higher temperature as the frequency increases. The relaxation follows an Arrhenius law with an activation energy $E \sim 0.24$ eV. This effect can be ascribed to charged defects inducing a Maxwell-Wagner type of interfacial polarization in agreement with Koop's two-layer model. Another contribution to the dielectric properties is the conduction mechanism of the polycrystalline CFO phase with temperature leading to an artificial increase of both the capacitance and losses at high temperature.

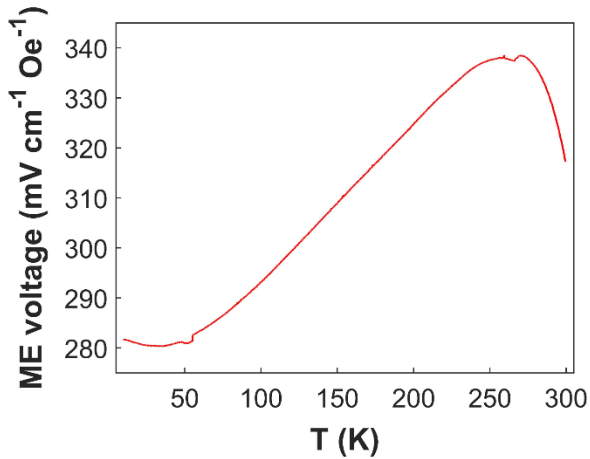


Figure 5. Temperature dependence of the ME voltage coefficient for the BSTO-CFO nanostructure.

This thermally activated process can be ascribed to the hopping of electrons between Fe^{2+} and Fe^{3+} or Co^{2+} and Co^{3+} ions. Such hopping mechanisms lead to local charge carrier displacement in the direction of electric field [24-26].

In the low temperature range ($T < 200$ K), for which the conductivity contribution can be neglected, the permittivity of the nanostructure ($\epsilon \sim 50$) is lower than the one of the pure BSTO film ($\epsilon \sim 150$) indicating the additional contribution of the low dielectric permittivity CFO phase.

In order to minimize the contribution at low frequency of space charge conductivity, ferroelectricity was probed by performing the capacitance-voltage (C - V) measurements at 1 MHz. The capacitance and dielectric losses measured at 190 K show two maxima with an opening of a hysteresis loop (figures 4(e) and 4(f)). In ferroelectric thin films, this is due to polarization reversal thus confirming the ferroelectric behaviour of our BSTO-CFO nanostructures. The same experiment performed at 290 K showed the progressive disappearance of the ferroelectric features and dominant paraelectric behaviour of the BSTO-CFO nanostructure in agreement with the diffuse ferroelectric-paraelectric transition around 250 K.

Direct measurement of the ME effect was performed to prove the magnetoelectric nature of the vertically aligned BSTO-CFO nanostructures and to provide a macroscopic estimation of the magnetoelectric coupling.

The temperature dependence of the ME voltage coefficient α_E in the range 10-300 K is shown in figure 5. The maximal value of the ME coefficient ~ 340 $\text{mV cm}^{-1} \text{Oe}^{-1}$ was observed

around $T \sim 250$ K. A decrease of the temperature between 250 K and 10 K leads to a reduction of the ME coefficient by ~ 17 %. The shape of the $\alpha_E(T)$ curve can be ascribed to the temperature dependence of the dielectric and magnetic properties of the multiferroic nanocomposite. Since the Curie temperature for bulk CFO ($T_C \sim 790$ K) is much higher than room temperature, the peak in the curve can be associated with the ferroelectric-paraelectric transition of the $\text{Ba}_{0.7}\text{Sr}_{0.3}\text{TiO}_3$ phase around $T_C \sim 250$ K, as illustrated in figures 4(c) and 4(e). In previous works performed on PZT- $\text{La}_{0.7}\text{M}_{0.3}\text{MnO}_3$ ($M = \text{Sr}, \text{Ca}$) multilayers and the PZT- $\text{La}_{1.2}\text{Sr}_{1.8}\text{Mn}_2\text{O}_7$ thin films, the highest ME coefficient values were observed around the Curie temperature of the ferromagnetic phase [27, 28].

The ME voltage coefficient of the BSTO-CFO heterostructure displays very small variation (of the order of 1 %) when the material is immersed within an external dc magnetic field (up to 4 T). The room temperature value of the ME voltage coefficient for the BSTO-CFO nanostructure (~ 320 $\text{mV cm}^{-1} \text{Oe}^{-1}$) is much higher than the values from macroscopic measurements reported earlier on (1-3) BFO-CFO composites [29-31], (in the range 20-74 $\text{mV cm}^{-1} \text{Oe}^{-1}$) and similar to that reported on (1-3) PZT-CFO composite (~ 390 $\text{mV cm}^{-1} \text{Oe}^{-1}$) [32]. It is further work to investigate the dependence of the magnetoelectric properties of such vertically aligned multiferroic heterostructures on geometrical factors and material parameters.

4. Conclusions

In this work, we developed an original and efficient pathway for the synthesis of vertically aligned multiferroic nanocomposites. The method allowed the fabrication of regular, dense and free-standing CoFe_2 nanopillar arrays by electrodeposition through an anodic aluminium oxide template supported on a Si substrate. Next, $\text{Ba}_{0.70}\text{Sr}_{0.30}\text{TiO}_3$ - CoFe_2O_4 multiferroic nanostructures were grown through direct rf sputtering deposition of a ferroelectric film on the pillar structure, with in-situ simultaneous oxidation of the ferromagnetic nanopillars, as confirmed by both structural and magnetic characterization. The synthesis approach preserves the morphology of the nanopillars during oxidation, improves the BSTO matrix penetration, and reduces the interface roughness between two constituents. The multiferroic

nanostructures exhibit strain-mediated ME coupling, whose maximum ME coefficient was measured as $\sim 340 \text{ mV cm}^{-1} \text{ Oe}^{-1}$ at around 250 K. Further optimisation of the fabrication process can be obtained by adjusting the magnetic packing fraction and pillar dimensions, thus opening a promising pathway towards versatile and controlled growth of vertically aligned multiferroic nanocomposites.

Acknowledgements

The IDS-FunMat European doctoral school is acknowledged for financial support. This work was partly supported by the Fédération Wallonie-Bruxelles (ARC 13/18-052, Supracryst) and by the Fonds de la Recherche Scientifique – FNRS under Grant n° T.0006.16. We are grateful to E. Lebraud for grazing incidence X-Ray diffraction measurements. Work at KU Leuven was supported by the Fund for Scientific Research – Flanders (FWO) and the KU Leuven Concerted Action (GOA/14/007).

References

- [1] Eerenstein W, Mathur N D and Scott J F 2006 Multiferroic and magnetoelectric materials *Nature* **442** 759-65
- [2] Nan C-W, Bichurin M I, Dong S, Viehland D and Srinivasan G 2008 Multiferroic magnetoelectric composites: Historical perspective, status, and future directions *J. Appl. Phys.* **103** 031101
- [3] Fiebig M 2005 Revival of the magnetoelectric effect *J. Phys. D: Appl. Phys.* **38** R123-52
- [4] Wang Y, Hu J, Lin Y and Nan C-W 2010 Multiferroic magnetoelectric composite nanostructures *NPG Asia Mater.* **2** 61-8
- [5] Bibes M and Barthélémy A 2008 Towards a magnetoelectric memory *Nat. Mater.* **7** 425-6
- [6] Bichurin M I, Petrov V M and Srinivasan G 2003 Theory of low-frequency magnetoelectric coupling in magnetostrictive-piezoelectric bilayers *Phys. Rev. B* **68** 054402
- [7] Zheng H, Wang J, Lofland S E, Ma Z, Mohaddes-Ardabili L, Zhao T, Salamanca-Riba L, Shinde S R, Ogale S B, Bai F, Viehland D, Jia Y, Schlom D G, Wuttig M, Roytburd A and Ramesh R 2004 Multiferroic $\text{BaTiO}_3\text{-CoFe}_2\text{O}_4$ nanostructures *Science* **303** 661-3
- [8] Zavaliche F, Zheng H, Mohaddes-Ardabili L, Yang S Y, Zhan Q, Shafer P, Reilly E, Chopdekar R, Jia Y, Wright P, Schlom D G, Suzuki Y and Ramesh R 2005 Electric field-induced magnetization switching in epitaxial columnar nanostructures *Nano Lett.* **5** 1793-6
- [9] Gao X, Rodriguez B J, Liu L, Birajdar B, Pantel D, Ziese M, Alexe M and Hesse D 2010 Microstructure and properties of well-ordered multiferroic $\text{Pb}(\text{Zr},\text{Ti})\text{O}_3/\text{CoFe}_2\text{O}_4$ nanocomposites *ACS Nano* **4** 1099-107
- [10] Liu M, Li X, Imrane H, Chen Y, Goodrich T, Cai Z, Ziemer K S, Huang J Y and Sun N X 2007 Synthesis of ordered arrays of multiferroic $\text{NiFe}_2\text{O}_4\text{-Pb}(\text{Zr}_{0.52}\text{Ti}_{0.48})\text{O}_3$ core-shell nanowires *Appl. Phys. Lett.* **90** 152501
- [11] Sallagoity D, Elissalde C, Majimel J, Maglione M, Antohe V A, Araujo F A, Pereira de Sá P M, Basov S and Piraux L 2016 Synthesis of dense arrays of multiferroic $\text{CoFe}_2\text{O}_4\text{-PbZr}_{0.52}\text{Ti}_{0.48}\text{O}_3$ core/shell nanocables *RSC Advances* **6** 106716-22
- [12] Parker C B, Maria J-P and Kingon A I 2002 Temperature and thickness dependent permittivity of $(\text{Ba},\text{Sr})\text{TiO}_3$ thin films *Appl. Phys. Lett.* **81** 340-2
- [13] Mátéfi-Tempfli S, Mátéfi-Tempfli M and Piraux L 2009 Fabrication of nanowires and nanostructures: combining template synthesis with patterning methods *Appl. Phys. A* **96** 603-8
- [14] Mátéfi-Tempfli S, Mátéfi-Tempfli M, Antohe V A and Piraux L Nanowires and nanostructures fabrication using template methods: a step forward to real devices combining electrochemical synthesis with lithographic techniques 2009 *J. Mater. Sci.: Mater. Electron.* **20** S249-54
- [15] Nielsch K, Choi J, Schwirn K, Wehrspohn R B and Gösele U 2002 Self-ordering Regimes of Porous Alumina: The 10 Porosity Rule *Nano Lett.* **2** 677-80
- [16] Encinas-Oropesa A, Demand M, Piraux L, Huynen I and Ebels U 2001 Dipolar interactions in arrays of nickel nanowires studied by ferromagnetic resonance *Phys. Rev. B* **63** 104415
- [17] Hua Z H, Chen R S, Li C L, Yang S G, Lu M, Gu B X and Du Y W 2007 CoFe_2O_4 nanowire arrays prepared by template-electrodeposition method and further oxidization *J. Alloy. Compd.* **427** 199-203
- [18] Dmytriiev O, Al-Jarah U A S, Gangmei P, Kruglyak V V, Hicken R J, Mahato B K, Rana

- B, Agrawal M, Barman A, Mátéfi-Tempfli M, Piraux L and Mátéfi-Tempfli S 2013 Static and dynamic magnetic properties of densely packed magnetic nanowire arrays *Phys. Rev. B* **87** 174429
- [19] Chinnasamy C N, Jeyadevan B, Shinoda K, Tohji K, Djayaprawira D J, Takahashi M, Joseyphus R J and Narayanasamy A 2003 Unusually high coercivity and critical single-domain size of nearly monodispersed CoFe_2O_4 nanoparticles *Appl. Phys. Lett.* **83** 2862-4
- [20] Cullity B D and Graham C D 2009 *Introduction to magnetic materials*, 2nd edn, ed L Hanzo (Hoboken, NJ: A John Wiley & Sons, Inc.) pp 141-83
- [21] Ojha S, Nunes W C, Aimon N M and Ross C A 2016 Magnetostatic interactions in self-assembled $\text{Co}_x\text{Ni}_{1-x}\text{Fe}_2\text{O}_4/\text{BiFeO}_3$ multiferroic nanocomposites *ACS Nano* **10** 7657-64
- [22] Tagantsev A K, Sherman V O, Astafiev K F, Venkatesh J and Setter N 2003 Ferroelectric materials for microwave tunable applications *J. Electroceram.* **11** 5-66
- [23] Lobo R P S M, Mohallem N D S and Moreira R L 1995 Grain-size effects on diffuse phase transitions of sol-gel prepared barium titanate ceramics *J. Am. Ceram. Soc.* **78** 1343-6
- [24] Jonker G H 1959 Analysis of the semiconducting properties of cobalt ferrite *J. Phys. Chem. Solids* **9** 165-75
- [25] George M, Nair S S, Malini K A, Joy P A and Anantharaman M R 2007 Finite size effects on the electrical properties of sol-gel synthesized CoFe_2O_4 powders: deviation from Maxwell-Wagner theory and evidence of surface polarization effects *J. Phys. D: Appl. Phys.* **40** 1593-602
- [26] Mahajan R P, Patankar K K, Kothale M B, Chaudhari S C, Mathe V L and Patil S A 2002 Magnetolectric effect in cobalt ferrite-barium titanate composites and their electrical properties *Pramana* **58** 1115-24
- [27] Srinivasan G, Rasmussen E T, Levin B J and Hayes R 2002 Magnetolectric effects in bilayers and multilayers of magnetostrictive and piezoelectric perovskite oxides *Phys. Rev. B* **65** 134402
- [28] Wu T, Zurbuchen M A, Saha S, Wang R-V, Streiffer S K and Mitchell J F 2006 Observation of magnetolectric effect in epitaxial ferroelectric film/manganite crystal heterostructures *Phys. Rev. B* **73** 134416
- [29] Yan L, Xing Z, Wang Z, Wang T, Lei G, Li J and Viehland D 2009 Direct measurement of magnetolectric exchange in self-assembled epitaxial $\text{BiFeO}_3\text{-CoFe}_2\text{O}_4$ nanocomposite thin films *Appl. Phys. Lett.* **94**, 192902
- [30] Oh Y S, Crane S, Zheng H, Chu Y H, Ramesh R and Kim K H 2010 Quantitative determination of anisotropic magnetolectric coupling in $\text{BiFeO}_3\text{-CoFe}_2\text{O}_4$ nanostructures 2010 *Appl. Phys. Lett.* **97** 052902
- [31] Amrillah T, Bitla Y, Shin K, Yang T, Hsieh Y H, Chiou Y Y, Liu H J, Do T H, Su D, Chen Y-C, Jen S-U, Chen L-Q, Kim K H, Juang J Y and Chu Y H 2017 Flexible multiferroic bulk heterojunction with giant magnetolectric coupling via van der waals epitaxy *ACS Nano* **11** 6122-30
- [32] Wan J-G, Weng Y, Wu Y, Li Z, Liu J-M and Wang G 2007 Controllable phase connectivity and magnetolectric coupling behavior in $\text{CoFe}_2\text{O}_4\text{-Pb(Zr,Ti)O}_3$ nanostructured films *Nanotechnology* **18** 465708